A large format, high-performance CCD sensor for medical x-ray applications

William Des Jardin, Chris Parks, Hung Doan, Neal Kurfiss, and Keith Wetzel
Eastman Kodak Company, Rochester, NY, 14650-2008 USA

Abstract

CCD image sensors have been utilized as the detectors in digital spot mammography for needle biopsy systems. The requirements of a detector for this application are large sensing area, large pixel size, moderate resolution, and low noise. A large area full-frame CCD image sensor has been developed that is 50 mm x 50 mm with 2084 x 2084 pixels. It is manufactured using a true two-phase, transparent gate, buried channel CCD process. The transparent gate process improves the quantum efficiency from 40 percent to 55 percent at 540 nm. The true two-phase CCD operates in accumulation mode for low dark current without compromising charge capacity. The sensor has two different output amplifiers optimized for either low signal applications or high dynamic range applications. At a 2 MHz pixel rate the dynamic range is 84 dB or 88 dB depending on which output amplifier is selected. The large sensor format allows the elimination of the demagnification requirement in digital spot mammography applications and may be useful for mid-field digital diagnostic systems.

Keywords: Digital spot mammography, Charge coupled device, CCD, image sensor, transparent gate.

Contents

1. INTRODUCTION

A common system configuration to provide real time digital detection of x-rays is a scintillator screen coupled to a CCD image sensor. The scintillator converts the x-ray photons to visible light that is detected by the CCD. The light from the scintillator can be coupled to the CCD using either a lens or a fiber optic bundle (FOB). Published analyses of the performance of these systems is available.[1,2] The throughput of the lens based system can be summarized as[1]

$$\eta_L = \frac{T(\lambda)}{1 + 4 \cdot f_{\#}^2 \cdot (1+m)^2} \tag{1}$$

where T is the transmission factor for the lens, $f_{\#}$ is the f-number of the lens, and m is the demagnification factor.

The efficiency of the fiber optic bundle-based system is dependent on the material properties of the glass fibers and can be expressed as[1]

$$\eta_{TFO} = NA_T^2 = \left(\frac{1}{m}\right)^2 \cdot \left(\frac{(n_2^2 - n_3^2)^{1/2}}{n_1}\right)^2 \tag{2}$$

where NA_T is the fiber numerical aperture, and n_1, n_2, and n_3 are the indices of refraction in air, core, and cladding, respectively. In either system configuration the demagnification required to match the size of the scintillator to the CCD degrades the performance by reducing the signal reaching the CCD. The system would be improved if the demagnification was reduced.

A scintillator screen of 50 mm x 50 mm is used in digital spot imaging for mammographic needle biopsies. It is often coupled to a an image sensor one quarter this size such as the *KODAK DIGITAL SCIENCE*™ KAF-1001 Image Sensor using a 2:1 reduction fiber optic taper. Figure 1 shows a cross section of the key components for this configuration. We have developed a sensor that will allow the demagnification requirement to be removed for the needle biopsy application. The sensing area is 50.0 mm x 50.0 mm, which will result in the configuration shown in Fig. 2. The sensor is built using a transparent gate CCD process[3] that increases the quantum efficiency at 540 nm by forty percent compared to other front side illuminated CCD sensors. The larger size and improved sensitivity will increase the system signal gathering capability by up to a factor of six. Another advantage is a lighter, and more compact system.

Figure 3 shows the completed CCD sensor. The sensor is fabricated using 150 mm silicon wafers that allow multiple sensors to be fabricated on each wafer. The two-phase full-frame CCD process is uncomplicated to manufacture and demonstrates good yield even for a sensor this large.

2. SENSOR ARCHITECTURE

Figure 4 is a functional block diagram of the sensor. It consists of 2084 photoactive rows and column of 24 μm square pixels. All of the shift registers in the sensor are true two-phase buried

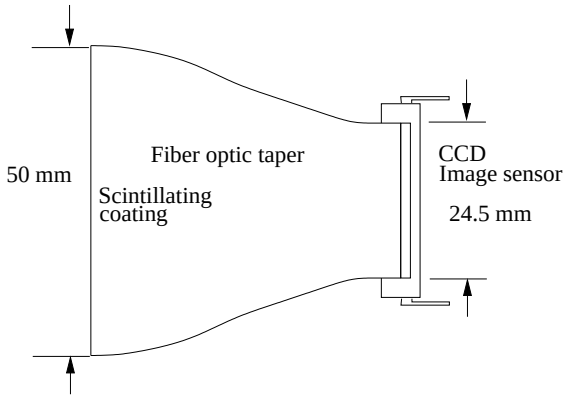

Figure 1. Fiber optically coupled CCD with demagnification.

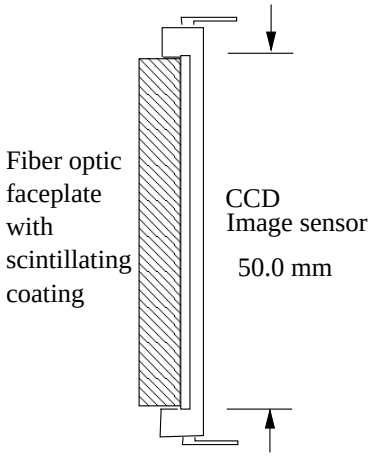

Figure 2. Fiber optically coupled CCD without demagnification.

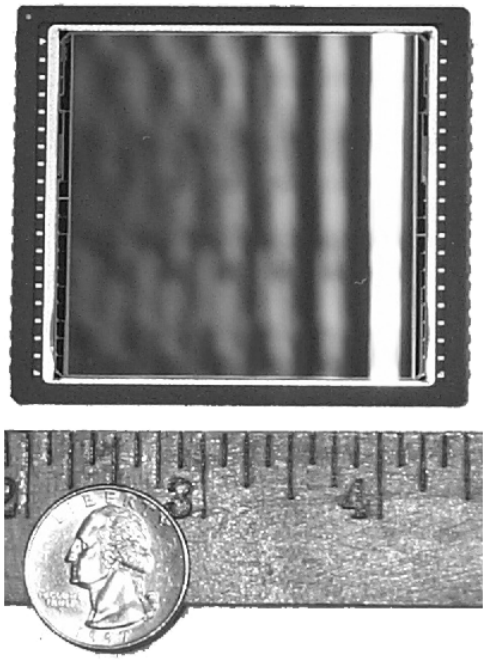

Figure 3. Photograph of the completed sensor.

channel CCDs arranged in a full-frame architecture.[4] The CCD gates act as both the photosensitive elements and the readout registers. Larger pixels can be formed through binning at the expense of resolution.

The photoactive area is surrounded by light shielded rows and columns that function as a dark reference. The image information is read a line at a time into a single, horizontal CCD shift register. The pixel information is then presented to one of two outputs. The sensor operates as a single output device, but the user has a choice of two different types of output amplifiers. One amplifier has a 10 μV/electron conversion factor for good sensitivity at low signals. The

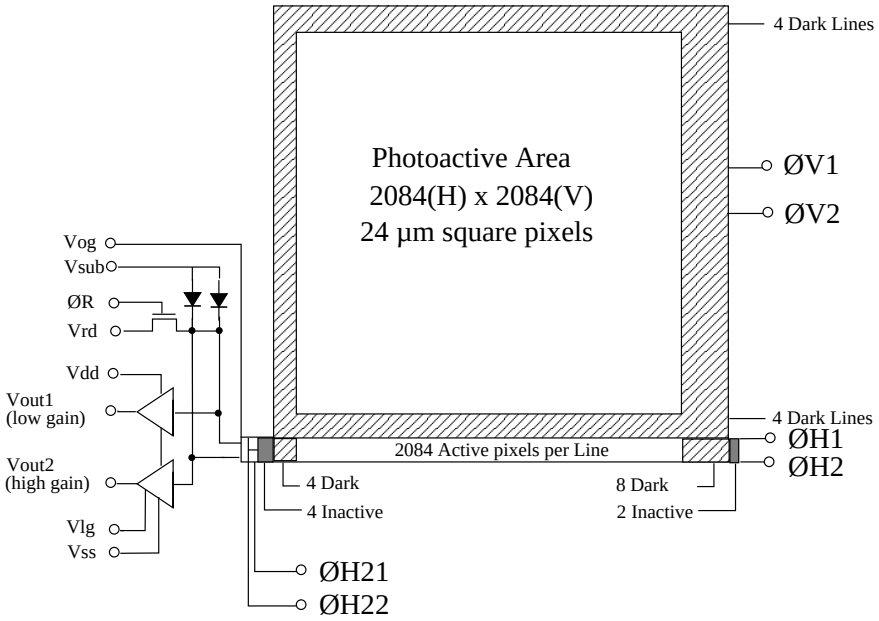

Figure 4. 2084 x 2084 sensor functional block diagram.

high conversion capability limits the largest signal to 200,000 electrons, which is less than half the charge capacity of each pixel. The other amplifier has a 2 μV/electron conversion factor that allows the full pixel charge capacity to be usable at the output.

3. PIXEL DESCRIPTION

The transparent gate process replaces the second polysilicon gate electrode with one made from indium tin oxide and significantly improves the spectral response of the pixel. During the readout clock sequence all of the signal must be contained under each of the gates separately and alternates between them. The maximum signal will be limited by whichever gate has the smaller capacitance. Each gate has the same capacitance per unit area so usually both gates are the same size so that the charge capacity is maximum. The large 24 μm pixel size of this sensor allows a trade off between increased sensitivity from enlarging the second, transparent gate and the decrease in charge capacity from the correspondingly smaller first poly silicon gate. Figure 5 shows the final pixel design. For this sensor a 10 μm long first gate results in adequate charge capacity of 550,000 electrons per pixel while allowing the second gate to have a larger, 14 μm gate length to maximize the effect of using the transparent electrode.

4. OUTPUT STRUCTURE

As mentioned previously, there are two types of output amplifiers on the sensor. There is a high gain, 10 μV/electron, two-stage source follower and a lower gain, 2 μV/electron, single-stage source follower. The last gate of the horizontal shift register is split to allow the charge to be directed to the desired output. Figure 6 shows a simplified diagram of this scheme. The ΦH2

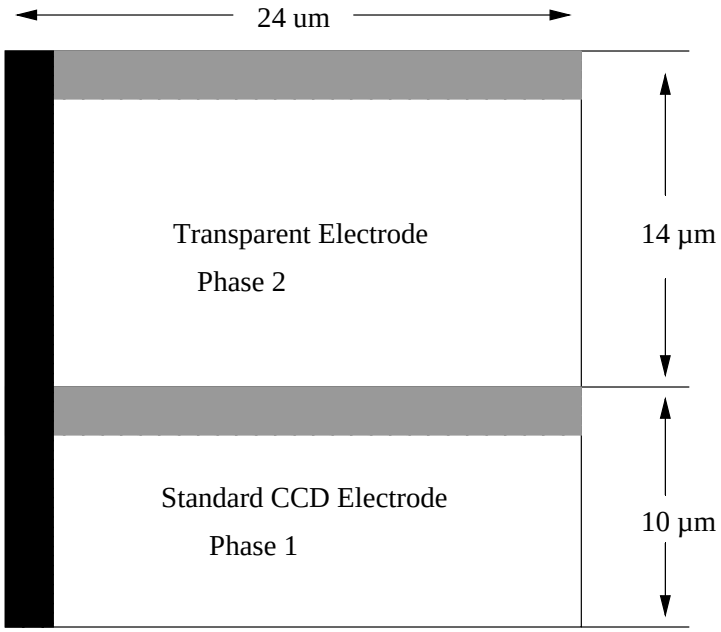

Figure 5. Details of pixel design.

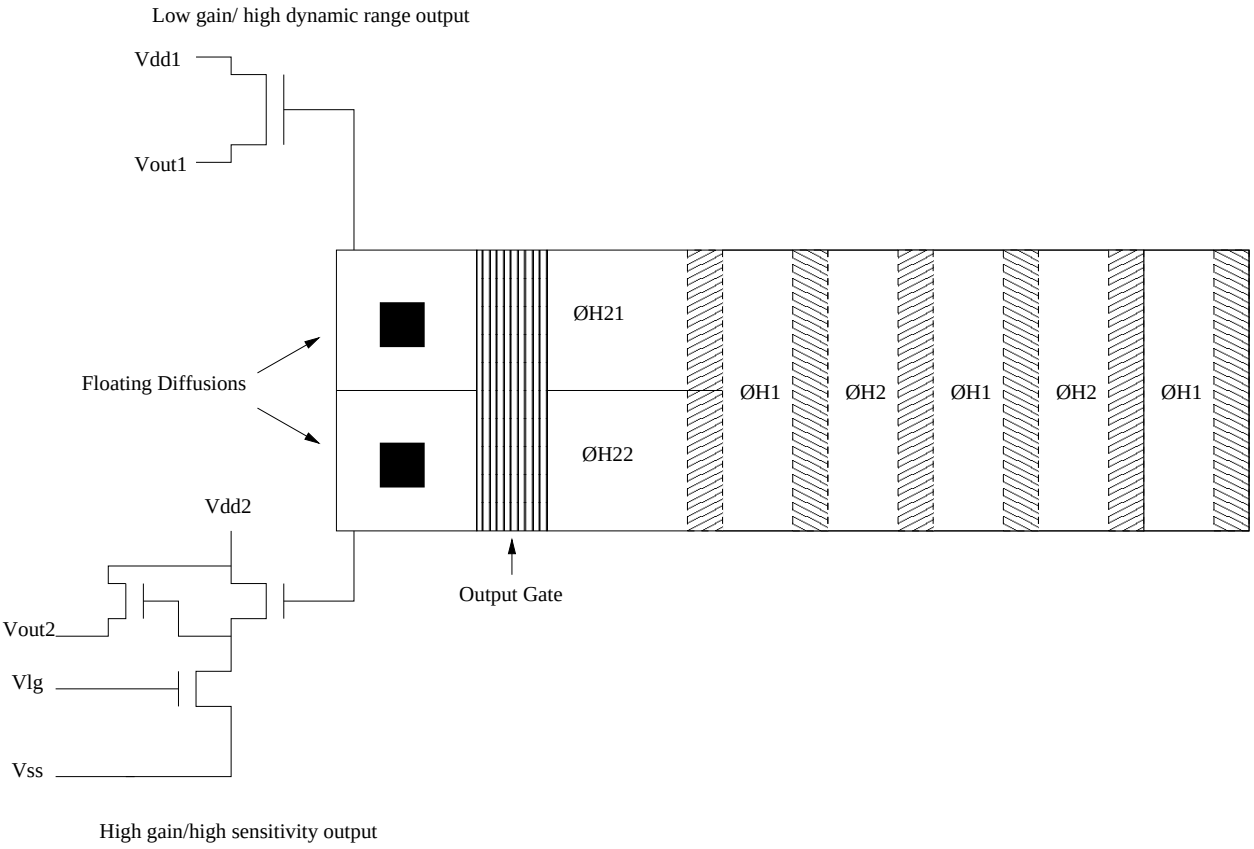

Figure 6. Details of output design.

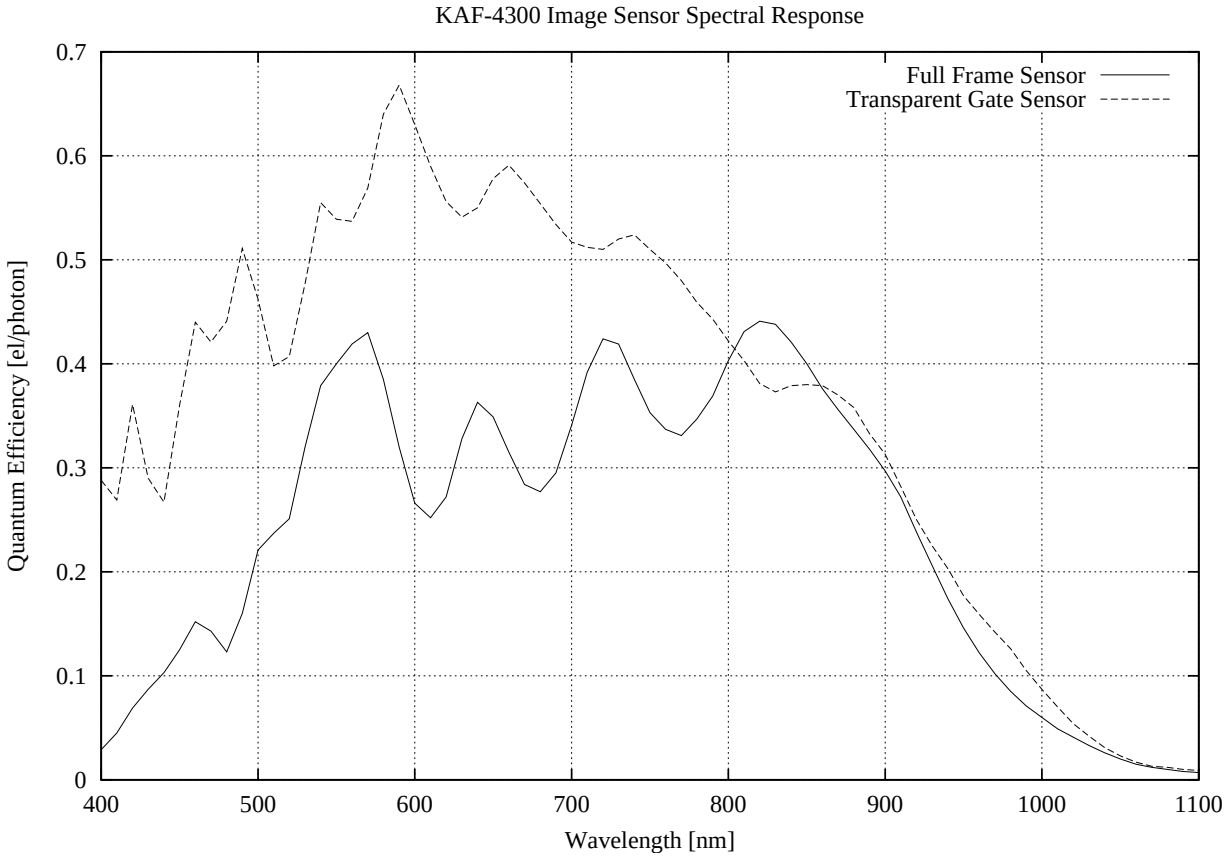

Figure 7. Full-frame CCD spectral response.

clock is applied to the gate associated with the output to be used, while the other side of the last gate is held to a static level that is the same as the low level of the ΦH2 clock.

5. PERFORMANCE

5.1. Spectral Response

The sensor has been fabricated using two different fabrication processes. One is the standard polysilicon gate full-frame CCD process and the other is an enhanced response transparent gate process. Figure 7 shows the spectral response of sensors made from each of these processes. Sensors from either process will improve the system response because of the better optical throughput from using a large detector. The transparent gate CCD sensor will improve it further.

5.2. Dark Current

The true two-phase CCD process produces shift registers that operate with accumulation mode or MPP timing.[3] During the integration time and most of the readout time both phases of the

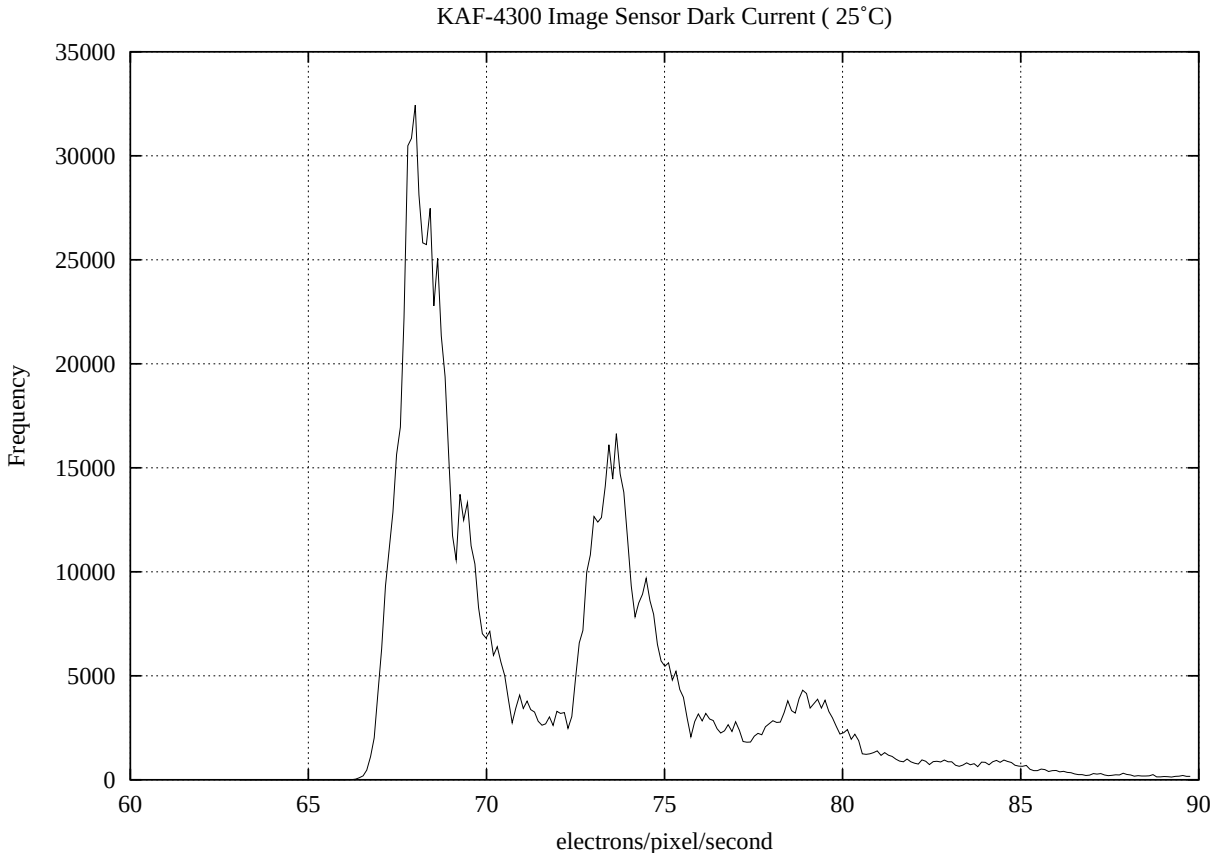

Figure 8. Sensor dark current histogram.

CCD clocks are held at a low level. When the clocks are at their low level the silicon-gate dielectric interface is accumulated with holes, which fill mid-gap states and suppress the surface state component of the dark current.

While the clocks are held in their low states the charge is divided between them. During the transfer of each line the clocks are alternately set to their high levels. All the charge is held under whichever gate is at the high level. At the end of the transfer of one line, the clocks return to the low state where the charge is again split between the two gates. The sharing of the charge while both clocks are low maintains a high charge capacity even when operating in a low dark current clocking mode.

The dark current was measured to be less than 10 pA/cm^2 or 360 electrons per pixel per second at 25°C. This dark current is primarily due to the generation in the depleted buried channel and diffusion current from the top epitaxial layer of the silicon substrate.

An example of a histogram of the dark current from one sensor is shown in Fig. 8. The histogram shows three distinct normal distributions. The distribution with the lowest dark current value is because of a uniform generation source (i.e., a generation source that affects every pixel). The next highest peak corresponds to pixels that contain one extra generation site caused by low-level metallic contamination.[5] The last prominent peak is from pixels that

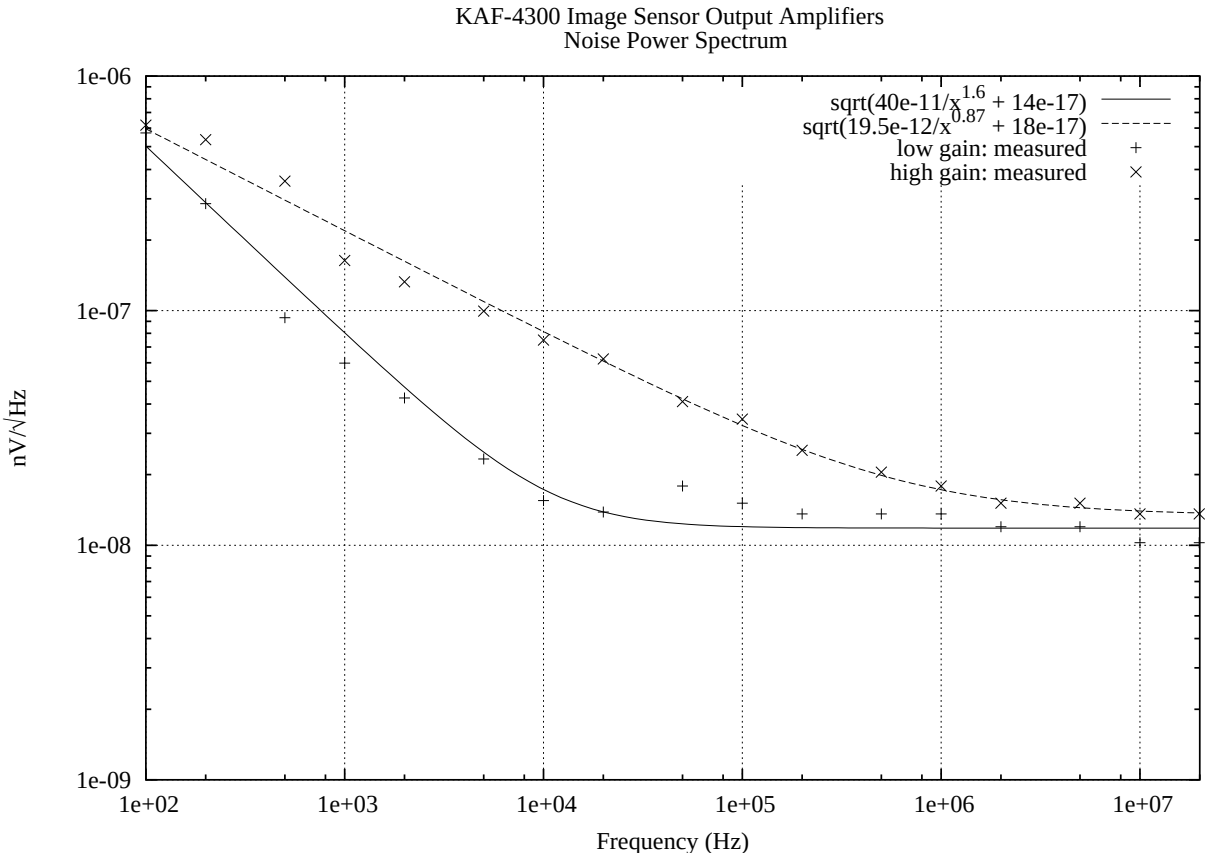

Figure 9. Output amplifiers noise power spectrum.

contain two of the extra generation sites. This type of dark current signature is observed when the surface dark current is negligible, and the contribution caused by the bulk diffusion current is small. This is common for sensors fabricated with the true two-phase full frame technology.

5.3. Noise

The signal noise is due to three contributions: shot noise on the photo generated signal, shot noise from the dark current, and the amplifier electronic noise. The lowest noise occurs in the dark where there is no photo generated signal shot noise. If the dark signal shot noise is minimized through cooling of the sensor then the output amplifier electronic noise floor will be the limiting noise component.

The final electronic noise floor is dependent on the analog processing circuitry, such as correlated double sampling and the system bandwidth. This noise floor can be calculated with knowledge of the operating frequency, analog bandwidth, and transfer functions of the processing circuit components.

An important input to this analysis is the noise power spectrum of the sensor output amplifiers. The noise power spectrum was measured using an HP3585A Spectrum Analyzer with the output amplifiers biased at their nominal operating point.

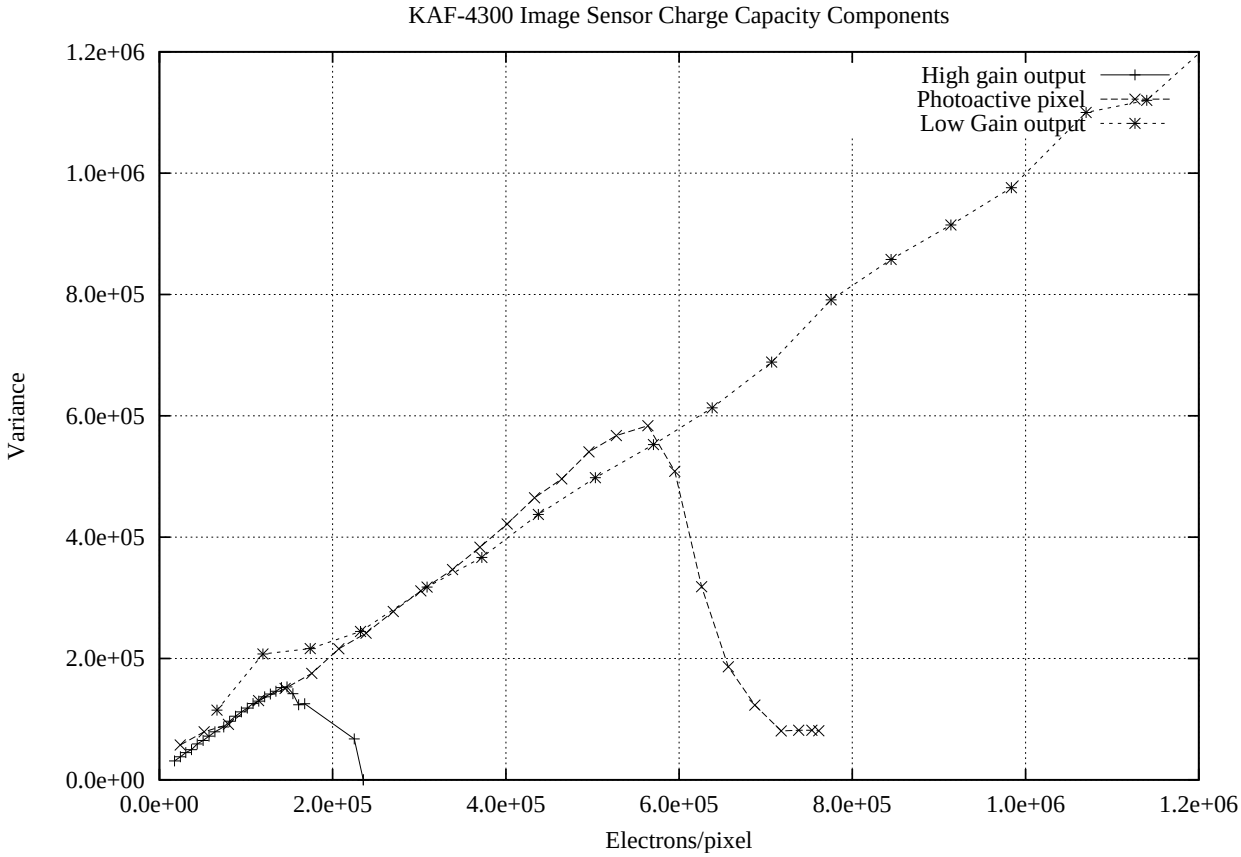

Figure 10. Charge capacity of various sensor components.

The results of these measurements are shown in Fig. 9 for both output amplifiers. The noise spectra show the typical MOS amplifier noise behavior of a $1/f$ dependence that approaches a constant white noise floor.[6] The low gain amplifier has a knee frequency of 20 kHz compared to 1 MHz for the high gain amplifier due to the geometry differences in their drive transistors. The low gain, single-stage amplifier has a single large drive transistor while the drive transistor of the first stage of the high gain amplifier is made small to maximize the charge to voltage conversion of the output node.

The white noise floor measured is close to the capability for the measurement system that was used and the values shown here may be limited by the measurement technique. The plot contains analytical representations of the noise floor behavior that can be used in the analysis of the system noise floor. The units of noise power spectrum are nV/$\sqrt{Hz}$. After processing the noise power, taking into account the transfer function of the analog processing and the bandwidth, the output noise can be input referred by applying the output conversion factor in μV/electron. A typical noise floor of 12 electrons has been demonstrated using the high gain amplifier, a 1 MHz pixel rate, and a 15 MHz analog bandwidth.

5.4. Charge Capacity

The sensor is composed of three main sections: the photoactive pixel, the serial readout register, and the output charge detection node. Knowledge of the charge capacity of each of these is necessary to understand the limitations of using the sensor in a particular application. The charge capacity of the sensor was determined by measuring the signal and noise while varying the exposure level. The point where the noise begins to decrease as the signal is increased is taken as the saturation point. At this point, there are mechanisms causing the noise to deviate from the theoretically expected shot noise result.

A summary of the measurements is shown in Fig.10. The lowest charge capacity was determined to be the charge conversion node of the high gain output. Using nominal operating conditions, a maximum output voltage of 1.5 volts or 150,000 electrons was achieved before the noise begins to decrease.

Switching to the low gain amplifier output allows the full charge capacity of the photoactive pixel (570,000 electrons) to be observed. The low gain amplifier output capacity was measured to be 1,000,000 electrons by operating the sensor in binning mode to generate signals greater than what one pixel could provide to the output.

The dynamic range of the output node can be increased by changing the bias conditions of the amplifiers so that a larger voltage swing can be accommodated. This is accomplished by increasing Vdd and Vrd, and adjusting the reset clock appropriately. The largest signal that was achieved was 1,750,000 electrons with Vdd = 17 volts, Vrd = 14 volts, and the reset clock operating between +2 and +12 volts. Even with adjusting the output for maximum voltage swing, the serial register capacity was never reached before the outputs saturated.

5.5. Charge Transfer Efficiency

Table 1. Charge transfer efficiency versus pixel rate.

Frequency (kHz)	CTE (%)
500	99.99963
1000	99.99967
2500	99.99782

Charge transfer efficiency (CTE) is a measure of the ability of the CCD shift register to move charge from one element to the next. It is reported in units of percent of the charge transferred compared to the original amount. A CTE equal to 99.9995% would result in a 2% loss for signals that are transferred the entire length of the serial shift register.

The charge transfer efficiency was measured at room temperature by integrating the sensor in the dark for several seconds and using pixels with excess dark current as the signal source. The charge transfer efficiency was calculated as:

$$CTE = 1 - \left(\frac{N_{c+1}}{N_c}\right) \cdot \left(\frac{1}{2 \cdot c}\right) \tag{3}$$

where N_c and N_{c+1} are the signal levels at column number c and $c+1$ respectively. The factor of two in the denominator of the last term is used to convert the efficiency per pixel to the efficiency per shift of a two-phase register. The data was collected concentrating on the highest numbered columns. These experience the most shifts and would be the most affected by the transfer efficiency. The transfer efficiency can be signal level dependent. As N_c is increased the CTE will also increase if the loss (N_{c+1}) is independent of signal level. The signals used for the measurement varied from 0.3% to 1.8% of the pixel charge capacity so that the results would reflect worst case operating conditions.

The results are presented in table 1 as a function of pixel frequency. The transfer efficiency was observed to be independent of the clock rate below 1 MHz. It was noticeably worse at 2.5 MHz. Above 2.5 MHz the quality of the image was severely impacted by the transfer inefficiency. At 1 MHz and lower the CTE will cause a maximum signal loss of less than 2%. Similar sensors using the same pixel design do not show a decrease in the CTE until 5 MHz. The transfer inefficiency observed for this sensor is probably due to unoptimized clock circuits driving the large capacitive load of the serial register on this sensor.

6. CONCLUSION

A large format CCD image sensor has been developed for medical x-ray applications. The large size reduces the amount of demagnification required to match the imaging and sensor areas. This results in a corresponding increase in the throughput of the optical system. The sensor has a large dynamic range, low noise floor, low dark current, and improved spectral response compared to other front side illuminated full-frame CCD sensors. Table 2 summarizes the features and performance of this sensor.

ACKNOWLEDGMENTS

The authors would like to thank the members of Image Sensor Solutions division of Eastman Kodak Company for the process development, fabrication, and testing of this sensor.

Table 2. *KODAK DIGITAL SCIENCE*™ KAF-4300 Image Sensor features and performance summary.

Parameter	Value
Image size	50 mm x 50 mm
Architecture	Full-frame CCD
Resolution	2084 x 2084
Pixel size	24 μm
Quantum Efficiency (540 nm)	55%[a]
Dark Current	< 10 pA/cm^2
CTE	$> 99.999\%$
Output Sensitivity	High gain output - 10 μV/electron
	Low gain output - 2 μV/electron
Noise floor	12 electrons[b]
Saturated signal	High gain output - 150,000 electrons
	Photoactive pixel - 550,000 electrons
	Low gain output - 1,000,000 electrons

[a] using transparent gate process
[b] 1 MHz; 15 MHz bandwidth

REFERENCES

1. S. H. and D. P. Trauernicht, "Potential image quality in scintillator CCD-based x-ray imaging systems for digital radiography and digital mammography" in Medical Imaging 1996: Physics of Medical Imaging, Richard L. Van Metter, Jacob Beutel, Editors, Proc. SPIE 2708, p. 440-449 (1996).
2. C. H. Slump, G. J. Laanstra, H. Kuipers, M. A. Boer, A. G. J. Nijmeijer, M. J. Bentum, R. Kemner, H. J. Meulenbrugge, R. M. Snoeren, " A novel X-ray detector with multiple screen CCD sensors for real-time diagnostic imaging" in Medical Imaging 1996: Physics of Medical Imaging, Richard L. Van Metter, Jacob Beutel, Editors, Proc. SPIE 2708, p. 450-461 (1996).
3. E. G. Stevens, S. L. Kosman, J. C. Cassidy, W. C. Chang, and W. A. Miller, "A large format 1280 x 1024 full-frame CCD image sensor with a lateral-overflow drain and transparent gate electrode", SPIE Proceedings, **1147**, p. 274-282, Feb., 1991.
4. E. G. Stevens, T-H Lee, D. N. Nichols, C. N. Anagnostopoulos, B. C. Burkey, W-C Chang, T. M. Kelly, R. P. Kosla, D. L. Losee, and T. J. Tredwell, " A 1.4 million element CCD image sensor," ISSCC Digest of Technical Papers, p. 114-115; Feb., 1987.
5. W. C. McColgin, J. P. Lavine, and C. V. Stancampiano, "Probing metal defects in CCD image sensors", Materials Research Society Proceedings, **378**, p. 713-724, 1995.
6. P. Gray and R. Meyer, *Analysis and Design of Analog Integrated Circuit*, John Wiley & Sons, New York, 1984.